ISSN 0016-7037
Volume 74, Number 20
October 15, 2010

Geochimica et Cosmochimica Acta

JOURNAL OF THE GEOCHEMICAL SOCIETY
AND THE METEORITICAL SOCIETY

Volume 74, Number 20 October 15, 2010

Articles

Continued on outside back cover

Available online at www.sciencedirect.com
ScienceDirect
Geochimica et Cosmochimica Acta 74 (2010) 5906–5925
Geochimica et Cosmochimica Acta
www.elsevier.com/locate/gca

Two diffusion pathways in quartz: A combined UV-laser and RBS study

P.L. Clay [a,b,*], E.F. Baxter [a], D.J. Cherniak [c], S.P. Kelley [b], J.B. Thomas [c], E.B. Watson [c]

[a] Dept. of Earth Sciences, Boston University, Boston, MA 02215, USA
[b] Dept. of Earth and Environmental Sciences, Centre for Earth, Planetary, Space and Astronomical Research, The Open University, Milton Keynes MK7 6AA, UK
[c] Dept. of Earth and Environmental Sciences, Rensselaer Polytechnic Institute, Troy, NY 12180, USA

Received 16 June 2009; accepted in revised form 6 July 2010; available online 18 July 2010

Abstract

The diffusive behavior of argon in quartz was investigated with three analytical depth profiling methods: Rutherford Backscattering Spectroscopy (RBS), 213 nm laser ablation, and 193 nm (Excimer) laser ablation on the same set of experimental samples. The integration of multiple depth profiling methods, each with different spatial resolution and sensitivity, allows for the cross-checking of methods where data ranges coincide. The use of multiple methods also allows for exploration of diffusive phenomena over multiple length-scales. Samples included both natural clear rock crystal quartz and synthetic citrine quartz. Laser analysis of clear quartz was compromised by poor coupling with the laser, whereas the citrine quartz was more easily analyzed (particularly with 193 nm laser). Diffusivity measured by both RBS and 193 nm laser ablation in the outermost 0.3 μm region of citrine quartz are self-consistent and in agreement with previously published RBS data on other quartz samples (including the clear quartz measured by RBS in this study). Apparent solubilities (extrapolated surface concentrations) for citrine quartz are in good agreement between RBS, 213 nm, and 193 nm laser analyses. Deeper penetration of argon measured up to 100 μm depth with the 213 nm laser reveal contributions of a second, faster diffusive pathway, effective in transporting much lower concentrations of argon into the crystal interiors of both clear and citrine quartz. By assuming such deep diffusion is dominated by fast pathways and approximating them as a network of planar features, the net diffusive uptake can be modeled and quantified with the Whipple–LeClaire equation, yielding δD_b values of 1.32×10^{-14} to 9.1×10^{-17} cm^3/s. While solubility values from the measured profiles confirm suggestions that quartz has a large capacity for argon uptake (making it a potentially important sink for argon in the crust), the slow rate of lattice diffusion may limit its capability to take up argon in shorter lived geologic environments and in experiments. In such shorter-lived systems, bulk argon diffusive uptake will be dominated by the fast pathway and the quartz lattice (including natural isolated defects that may also be storing argon) may never reach its equilibrium capacity.

1. INTRODUCTION

1.1. Argon diffusion in quartz

In this study we seek to investigate the potential role of quartz as a 'sink' mineral for argon (and by analogy, perhaps for the other noble gases) as hypothesized recently in field based (e.g., Baxter et al., 2002) and experimental

* Corresponding author at: Dept. of Earth and Environmental Sciences, Centre for Earth, Planetary, Space and Astronomical Research, The Open University, Milton Keynes MK7 6AA, UK. Tel.: +44 01908 655947.
E-mail address: P.Clay@open.ac.uk (P.L. Clay).

0016-7037/$ - see front matter © 2010 Elsevier Ltd. All rights reserved.
doi:10.1016/j.gca.2010.07.014

(e.g., Watson and Cherniak, 2003) studies. Quartz would be an effective sink for argon if, (1) the solubility of argon in quartz relative to the solubility of surrounding phases (i.e., partitioning) is high, and (2) if the diffusivity of argon into quartz is high enough to permit argon to enter the quartz over available timescales. However, apparent discrepancies have been identified when comparing the experimental studies of Watson and Cherniak (2003) and Thomas et al. (2008) to that of Roselieb et al. (1997) whose studies suggest argon diffusivity and solubility in quartz differ by several orders of magnitude. This apparent discrepancy may be because these studies approached the question of argon diffusivity and solubility from different experimental and analytical directions: Watson and Cherniak (2003) and Thomas et al. (2008) used Rutherford Backscattering Spectroscopy (RBS) to measure diffusive uptake profiles in quartz at the 10's of nanometer scale, while Roselieb et al. (1997) used bulk analysis and electron microprobe.

While the absolute solubility limit for argon in quartz would rarely be reached in nature (i.e., there will rarely be enough argon in a natural system to saturate quartz), the parameter of greater importance is the partitioning of argon between quartz and other available system phases (e.g., minerals, fluids, grain boundaries). In this regard, the disparate conclusions of Watson and Cherniak (2003) and Thomas et al. (2008) to Roselieb et al. (1997) lead to different partition coefficients when compared to existing solubility data for other minerals. As this study highlights, depending upon the analytical method used, very different apparent diffusivities and apparent solubilities may be determined on the same mineral specimens. This shows the challenges in using existing solubility data measured by different methods to calculate mineral–mineral partition coefficients.

This is the first time a dual-study using both RBS and 193/213 nm UV-laser ablation mass spectrometric analyses has been undertaken on the same mineral samples, which illuminate heretofore unrecognized complexities in quantifying argon diffusivity. In comparing these three analytical methods, we are able to identify the presence of two distinctly different diffusive pathways in quartz. We interpret these two pathways as (1) slow lattice diffusion and, (2) fast-path diffusion that may be controlled by extended defects, dislocations or internal crystal imperfections. While our study focuses on quartz, the analytical lessons and noble gas behaviors learned here may well inform us about similar issues affecting the measurement of argon diffusivity solubility in other minerals, (e.g., Watson et al., 2007) concerning the long term storage of argon in the solid earth.

1.2. Background: fast-path and multi-diffusion

An understanding of the diffusion mechanisms by which geochronologically significant isotopes (e.g., Ar, He) are transported over geologically relevant timescales is crucial to geochronologic interpretations. It is likely because of this, that studies to quantify argon diffusion in minerals have been numerous (e.g., Foland, 1974; Giletti, 1974; Gilleti and Tullis, 1977; Harrison, 1981; Harrison et al., 1985; Wartho et al., 1999; Watson and Cherniak, 2003; Thomas et al., 2008). In the past (Turner, 1968; Schärer and Allègre, 1982), mechanisms of volume diffusion have been studied indirectly through geochronologic investigations concerning both single crystals and bulk mineral separates.

With the advent of high-resolution micro-sampling techniques, maps of intergrain spatial distribution of geochronologically important isotopes can be obtained. Some (Scaillet et al., 1990; Kelley and Turner, 1991; de Jong et al., 1992; Hames and Hodges, 1993; Hodges et al., 1994; Watson and Cherniak, 2003) found that most of their samples adhered to volume diffusion, resulting in concentration profiles interpretable in terms of simple diffusion through the crystalline lattice. Some studies (Phillips and Onstott, 1988; Onstott et al., 1991; Scaillet et al., 1992; Kelley et al., 1994), however, determined that samples yielded distinct concentration gradients, reflecting a mechanism other than volume diffusion. Crystal defects (microstructural defects, edge/screw dislocations, micro-fractures, nanopores, etc.) have been shown to allow for 'enhanced' or fast-path diffusion (Smoluchowski, 1952; Hart, 1957; Harrison, 1961; Le Claire, 1963; Ruoff and Baluffi, 1963; Balluffi, 1970; Le Claire and Rabinovitch, 1984; Lee, 1995).

Most early work towards quantification of diffusion rates within "fast paths" used measurements from low-angle grain-boundary diffusion rates (Whipple, 1954; LeClaire and Rabinovitch, 1984), relying on the assumption that the transport along dislocations can be related to the transport along an equivalent grain boundary slab, whereby the cross-sectional area of the grain boundary slab is equivalent to the sum of the area of the dislocations. LeClaire and Rabinovitch (1981, 1982, 1983, 1984) considered the diffusion into and along isolated, individual dislocations.

Potential fast-paths through which rapid diffusion can occur have been observed in different minerals (Veblen and Buseck, 1980; Skrotzki, 1990; Worden et al., 1990; Hacker and Christie, 1991; Dohmen et al., 2002; Zhang et al., 2006), and as a result, multiple diffusion pathways have been investigated in detail (Veblen and Buseck, 1980; Yund et al., 1981, 1989; Yurimoto and Nagasawa, 1989; Yurimoto et al., 1989; Skrotzki, 1990; Worden et al., 1990; Hacker and Christie, 1991). Many studies have tried to quantify how "fast-path" diffusion operates in minerals, and particularly, what the geologic significance of such a path may be.

The geo- and thermochronologic implications of fast-path diffusion may be significant. Most natural crystals will inherently have defects and dislocations (e.g., due to varying degrees of deformation) and it is feasible that any measurement of bulk diffusion through a crystal lattice will have some contributed effect from fast-path diffusivity through such networks. This fast path may be less significant in areas of low-defect density, or when temperatures are sufficiently high (or similarly, when timescales are long enough) for effective bulk lattice diffusivity. However, in shorter-lived, low-temperature systems and in defect-rich crystals, diffusion along these fast-paths or pipes may be an important process which warrants consideration. In this study, we present a unique integrated dataset which documents the existence of two diffusion pathways in quartz

and permits us to separate and quantify their relative contributions.

2. MATERIALS AND METHODS

2.1. Sample preparation

Two different quartz samples were used: a clear, natural rock crystal (used in the study of Watson and Cherniak, from Ward's Natural Scientific Establishment; referred to as clear quartz and samples denoted, N), and a synthetic citrine quartz (referred to as citrine quartz and samples denoted, SC). The citrine quartz is a synthetically-grown quartz sample (obtained from Facet Rough – Rock Peddler, www.rockpeddler.com) and was grown in a heated, pressurized autoclave, from seeds of natural rock crystal, typically over a period of months. Initial argon concentrations in untreated sample splits were measured and found to be negligible, at: 0.0180 ± 0.0032, 0.0052 ± 0.0041 and 0.0123 ± 0.0041 ppm argon within a short depth profile in the citrine quartz and similarly for the clear quartz at 0.0299 ± 0.0072, 0.0015 ± 0.0005 and 0 ppm argon. The clear quartz is the same as that used in Watson and Cherniak (2003), where the presence of localized patches of fluid inclusions was documented. Such inclusions are typically unavoidable due to their small size (down to 10–20 nm or less; see Watson and Cherniak, 2003 for discussion). The clear quartz samples were pre-annealed at 1000 °C for 3–7 days prior to polishing. This annealing procedure it negates any influence that the presence of hydrous species in the quartz lattice may have on argon diffusion and uptake into the quartz lattice (Watson and Cherniak, 2003). Electron microprobe data on the citrine quartz suggest that the crystal is chemically homogenous, however some heterogeneity in color within the citrine may indicate slight variations in Fe content, or ferrous/ferric ratios. No fluid inclusions in the citrine were observed optically or during electron microprobe analyses, however, due to the hydrothermal synthesis of the citrine quartz, it must be assumed that fluid inclusions are present on a small scale. Commercial, synthetically-grown quartz is changed to 'citrine' quartz through the addition of ferric iron impurities. This Fe is present in the quartz lattice in trace quantities (citrine quartz is 99.8% SiO_2). The presence of even trace Fe in the citrine is potentially noteworthy, as the study of Thomas et al. (2008) documented higher argon concentrations in the Fe-bearing minerals enstatite and San Carlos olivine than the pure end-member compositions, suggesting that oxidation of Fe could cause points defects and thereby enhance uptake of argon.

The citrine quartz was cut and polished using a low-speed Buehler Isomet precision diamond-blade saw. Chips were then mounted in epoxy and polished using Milli-Q water and 60 to 1 μm polishing papers. Samples were removed from the epoxy using an acetone bath and then cleaned ultrasonically in ethanol and de-ionized water. Pre-annealed, $3 \times 3 \times 1$ mm cuts of clear quartz were prepared from the study of Watson and Cherniak (2003) and were polished in the same manner as the citrine quartz cuts. No information on the crystallographic orientation of the samples was recorded following the study of Watson and Cherniak (2003) which demonstrated that crystallographic orientation does not strongly affect diffusivity.

2.2. Experimental procedure

Argon diffusion in quartz was investigated using "in-diffusion" experiments. The polished mineral samples were loaded into a ceramic tray, which was inserted into a cold-seal pressure vessel and furnace. The vessel was pressurized at 160–170 MPa with pure argon gas. During the experiment, samples are bathed in this pressurized argon atmosphere allowing argon to diffuse into the polished sample surface. Each cold-seal run can hold approximately 16–20 minerals. Each location within the sample tray (four containers per tray, each containing 4–5 minerals) is independently monitored with a thermocouple which records the temperature within a few millimeters of the sample. Temperature is known to within approximately ±2 °C. A thermal gradient present along the vessel allowed for four distinct temperature environments during the course of a single experiment (Table 1).

Two experiments were conducted in this study: the first at 170 MPa and a temperature range of 824–489 °C over a duration of 480 h and the second at 160 MPa, a temperature range of 724–419 °C over a duration of 360 h. The first experiment contained clear quartz, the second contained both clear and citrine quartz. Experiment details and run conditions (pressure, temperature and duration) are listed in Table 1. Each experiment was run with not only multiple samples of quartz, but also other silicate minerals including plagioclase feldspar, K-feldspar and phlogopite, in order to allow for the calculation of partition coefficients between these phases. However, because of unavoidable isobaric interferences of Ca and K on ^{40}Ar, RBS analysis could only be performed on quartz, which is the focus of this contribution. Data from feldspar experiments will be reported in a separate contribution.

Table 1
Experiment conditions. Cold-seal run conditions for two experiments in this study. "N" refers to natural clear quartz. "SC" refers to synthetic citrine quartz.

Sample	T (°C)	P (MPa)	Duration (h)
Experiment #1			
N1	824	170	480
N2	764	170	480
N3	642	170	480
N4	489	170	480
Experiment #2			
N5	724	160	360
SC-1	724	160	360
N6	669	160	360
SC-2	669	160	360
N7	561	160	360
SC-3	561	160	360
N8	419	160	360
SC-4	419	160	360

2.3. Analytical techniques and data acquisition

For all quartz samples, we employed RBS and 213 and/or 193 nm UV-laser ablation depth-profiling techniques to investigate diffusion of argon occurring over different length-scales within the crystal lattice. Details of all three analytical techniques are reviewed below.

2.3.1. Argon depth profiling: Rutherford Backscattering (RBS)

Non-destructive RBS analysis was undertaken first, providing information about argon concentrations within the outer ~100 nm of the crystal lattice. Full details of the RBS method are presented in Watson and Cherniak (2003). Quartz is well suited for RBS as there are no mass interferences on argon, as is often the case with other crustal silicate minerals – in particular those bearing significant potassium or calcium. The strength of the RBS method is the spatial resolution, which can be a few nanometers to 10's of nanometers. This fine spatial resolution illuminates features in the outermost portions of the quartz lattice that would be blurred or obscured by more crude techniques. The limitation of RBS, however, is the sensitivity. Argon concentrations below a few hundred ppm fall into the background noise of RBS. This technique has been used in previous studies of argon diffusion in minerals, including quartz (e.g., Watson and Cherniak, 2003; Thomas et al., 2008).

2.3.2. Argon depth profiling: UV-laser ablation mass spectrometry

After RBS analysis, two UV-laser ablation depth-profiling techniques were undertaken, including 213 nm laser measurements, followed later by 193 nm laser measurements on one citrine quartz sample only (see Section 2.3.5). 213 nm laser ablation of the quartz surface was accomplished by rastering the beam over a fixed area, removing one thin layer at a time, with increasing depth into the sample (Fig. 1). Depending on the laser conditions used and the material ablated, the depth of each layer ranged from 0.2 to 10 μm; this dimension determines the spatial resolution of the technique. The benefit of UV-laser ablation combined with noble gas mass spectrometry is the sensitivity to low argon concentrations. For the rastered layer volumes used in our samples, the detection limit was approximately 0.02 ppm argon (or about 1.12×10^{-5} cc-STP/g during analyses). This technique has been used in previous studies and described at length in Arnaud and Kelley (1995), Wartho et al. (1999) and Wartho et al. (2005). All measurements were undertaken using a MAP-215-50 noble gas mass spectrometer.

A "surface stripping" (Fig. 1) technique was used to remove the uppermost argon-rich layer of the mineral, in order to prevent interference with later measurements of argon concentrations from deeper within the lattice. In this study, the surface strip was removed (over an area of 300 μm^2), but argon concentrations released from this strip could not be measured because the high amount of argon present exceeded the limit of the mass spectrometer's detectors (but see below). Subsequent layers in the depth profile were over an area of 200 μm^2, precluding the possibility that these analyses might have clipped and incorporated some of the surface layer.

In order to quantify the argon concentrations within the surface layer removed in this style of analysis, a smaller surface area measurement was made on each sample where the argon released could be measured within the limits of the detectors. For most samples, a linear trough 5×100 μm was used. These measurements were used to provide information about concentrations within the uppermost surface of the mineral. Such measurements would technically include both contributions from any absorbed argon on the surface (if present) as well as argon within the outermost layer of quartz.

2.3.3. UV-laser ablation: citrine quartz vs. clear quartz

Disparate responses to the 213 nm UV-laser were observed between the citrine quartz and the clear quartz. Due to its optically-clear nature, the clear quartz did not couple strongly with the laser and ablation occurred by damage and fracture as much by ablation. Evidence of this fracturing is seen in the pit dimension measurements (see Section 2.3.4) of the clear quartz, where the excavated pits are jagged, non-uniform and exhibit evidence of fracturing and remaining debris (Fig. 1). Our later discussion takes into consideration the proportion of material outgassed

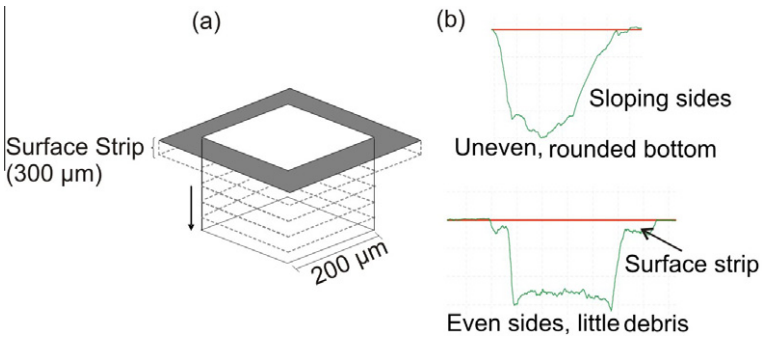

Fig. 1. (a) Illustration of laser ablation pits as measured by the Talysurf, the technique used for 213-nm laser pit measurements, resulting in profiles seen in (b). The 300 μm surface strip removal is seen at the mineral surface, with subsequent 200 μm ablation squares continuing at depth into the sample. Profiles for clear quartz (upper) and citrine quartz (lower) are shown in (b), illustrating the differences in the way the laser couples with different quartz samples (see Section 2.3.4).

relative to the volume of material excavated and whether or not 213 nm UV-laser analysis is suitable for this particular quartz variety.

Conversely, the citrine quartz coupled with the UV-lasers (213 nm and 193 nm; see Section 2.3.5 below) efficiently with no apparent fracturing and little or no edge fracturing in the excavated pits (Fig. 1). The citrine also appears to yield a consistent, reproducible amount of ablated material in each layer measured, and a desirable flat-bottomed pit.

2.3.4. 213 nm laser pit dimension measurements: Talysurf analysis

In order to calculate argon concentrations present in the ablated quartz, the volume of ablated material was calculated from measured pit dimensions using a Taylor Hobson "Talysurf II", which employs a diamond stylus mounted to a piezometer to raster along the bottom of the ablated pit or troughs and measure the pit dimensions. The Talysurf is capable of 0.1 μm precision. The limitation here occurs when the depth of the pit is greater than twice the width of the pit, as the stylus cannot achieve measurements of the true bottom. To avoid this problem, sufficiently large and/or shallow pit dimensions were used.

2.3.5. Additional argon depth profiling: ArF 193 nm Excimer laser ablation

In order to complement the spatial resolution limitations of the 213 nm laser, laser ablation profiles were performed at greater spatial resolution on synthetic citrine sample SC-1 (samples denoted in text and tables as five profiles, SC-E1 to SC-E5). Samples were ablated using a UP-193 nm ArF Excimer laser, in order to achieve fine-resolution, flat-bottomed laser pits. Samples were ablated repeatedly using as few as two 10 ns pulses at 0.5 mJ energy to achieve depth profiles. Final depths were measured using a Zygo white light interferometer. All pits exhibited depth variations but these were less than 0.05 μm and thus we have assigned this error to the individual pit depth measurements. Argon concentrations were calibrated using similar pits ablated in the international standard FCT sanidine. Measurements were undertaken using a Nu Instruments Noblesse noble gas mass spectrometer and automated extraction line.

3. DATA

Depth profiling data sets for each mineral sample include two concentration versus depth profiles; one from RBS and one from 213 nm UV-laser ablation. For sample SC-1, two sets of UV-laser ablation profiles exist from 213 nm laser analyses and from further 193 nm (these five profiles from sample SC-1 are denoted SC-E1 to SC-E5) laser analyses. All RBS, 213 nm- and 193 nm-laser data are available in a Supplementary online data appendix.

3.1. RBS data

A compilation of the clear and citrine quartz RBS diffusion profiles is given in Fig. 2. The most notable features of the profiles are the high concentrations seen (1000's of ppm) and shallow diffusive depth-scale (~ from 60 to nearly 250 nm), with measurable profiles reaching only a maximum of a few 100 nm into the crystalline lattice. There is a significant range in maximum surface concentration from sample to sample (ranging from 1050 to 13,450 ppm), and a fairly smooth and clear diffusional uptake profile emerges in each analysis. Citrine quartz generally shows higher maximum surface concentrations (7120 ± 100 to $13{,}450 \pm 200$) than clear quartz (1050 ± 100 to $10{,}050 \pm 200$). Diffusion and concentration data for RBS analyses are detailed in Table 2. Maximum surface concentrations in clear quartz are consistent with the study of Watson and Cherniak (2003), but much higher than Roselieb et al. (1997). This is not unexpected as we employ the same method (RBS) and used the same clear quartz starting material as Watson and Cherniak (2003).

3.2. 213 nm UV-laser data

The argon diffusion profiles measured using a 213 nm UV-laser to ablate samples in clear and citrine quartz exhibit significant variability in concentration, depth and shape (Table 3). A compilation of 213 nm laser data for clear and citrine quartz is given (Fig. 3). These profiles exhibit the key features seen in the laser measured profiles, including: (1) ~10's up to 150 μm depth of detectable argon penetration into the sample with argon concentrations ranging from 0.04 to 55 ppm in the clear quartz and 0.21 to 27 ppm in the citrine quartz, (2) a markedly higher surface concentration (e.g., up to 3012 ppm for SC-1; surface concentrations not shown on Fig. 3 due to drastically different concentration scales), (3) a sharp kink in the diffusive uptake profile slope as defined by the higher surface concentration point and subsequent one to two near-surface points (shown, for example, in Fig. 3a, occurring between 10 and 20 μm depth) and (4) considerable and variable scatter in the data.

A comparison of laser concentration-depth profiles for citrine and clear quartz can be made (Fig. 3a, b and c). The profiles exhibit different characteristics, with the clear quartz revealing lower argon concentrations, deeper penetration and more variable profiles, while the citrine quartz shows higher argon concentrations, considerably more smooth and well-behaved profiles, with shallower penetration into the crystal.

3.3. 193 nm UV-laser data

Sample SC-1 (724 °C, 160 MPa, 360 h) was selected for further laser ablation experiments using an ArF 193 nm laser. The 193 nm laser coupled well with the citrine quartz, yielding smooth flat bottom pits, and permitting much finer scale depth profiling with depth resolution as good as 0.06 μm per analysis. Five argon diffusion profiles were measured in this sample, revealing diffusion profiles with similar depths of penetration but with significant scatter in the maximum surface concentrations of argon. Concentrations ranged between 260 and 8792 ppm argon (measured). Laser profiles SC-E1, SC-E2, SC-E4 and SC-E5 (Fig. 4a, b, d and e) show a kink in the diffusional uptake profile labeled as 'kink point' on each profile. Laser profile SC-E3 (Fig. 4c) show uptake patterns that do not indicate an obvious kink.

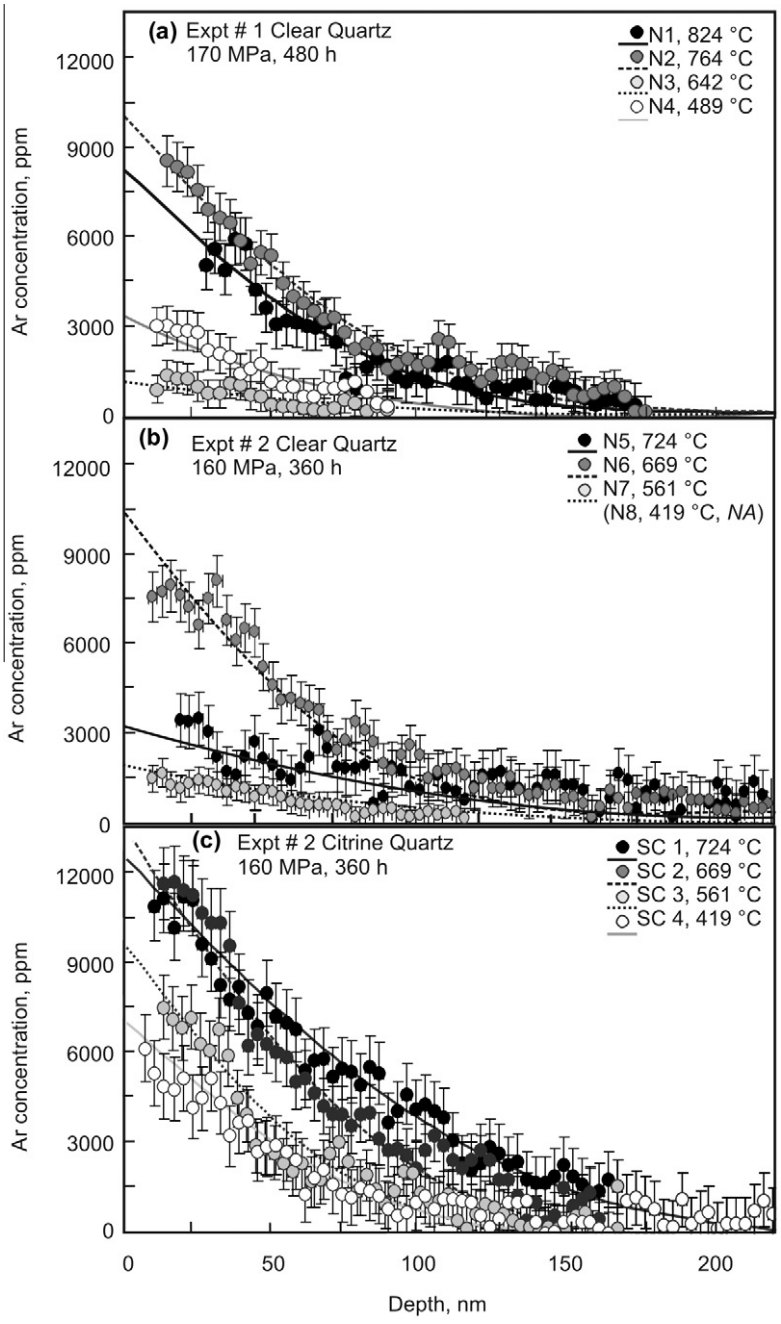

Fig. 2. RBS measured argon concentration (ppm) vs. depth (nm) profiles for clear quartz (expt. #1) samples N1–N4 (a); clear quartz (expt. #2) samples N5–N7 (b); and citrine quartz, samples SC-1 to SC-4 (c). Symbols given in the legend.

SC-E1 (Fig. 4a) shows an unexpected drop in concentration at the surface, as if some post-experimental loss of argon from the nearest surface had occurred. How this could be the case for this profile but not for the other four in this same mineral is unclear; we consider the nearest surface point in profile SC-E1 anomalous and disregard it.

4. DATA EXTRACTION: DIFFUSION MODELING APPROACHES FOR ARGON DEPTH PROFILES

Below, the methods used to model these profiles in order to quantify diffusivity in each case, are described.

4.1. Modeling lattice diffusion

The simplest argon uptake behavior would be pure lattice diffusion. Diffusion of argon is treated as 1-dimensional diffusion into semi-infinite planar medium, with a concentration-independent diffusivity. Diffusivities were thus obtained by fitting the profiles to the appropriate diffusion equation (Crank, 1975):

$$C = C_o\left[erfc\left(\frac{x}{\sqrt{4Dt}}\right)\right] \quad (1)$$

Table 2
Quartz RBS data. Extrapolated diffusivities and equilibrium concentrations for all quartz samples measured by RBS analysis. Errors on log D were taken to be 0.6 log units (Watson and Cherniak, 2003). R^2 values represent the goodness of the error-function fit to the data.

Sample	T (°C)	P (MPa)	Log D	R^2	Ar PPM	Ar (cc-STP/g-bar)
N1	824	170	−20.9	0.92	8000 ± 150	0.00263
N2	764	170	−20.8	0.93	9750 ± 250	0.00321
N3	642	170	−20.9	0.76	1050 ± 100	0.00034
N4	489	170	−21	0.91	3200 ± 300	0.00105
N5	724	160	−20.1	0.65	2950 ± 200	0.00103
SC-1	724	160	−20.4	0.98	12500 ± 150	0.00437
N6	669	160	−20.7	0.93	10050 ± 200	0.00351
SC-2	669	160	−20.7	0.91	13450 ± 200	0.0047
N7	561	160	−20.9	0.94	1800 ± 100	0.00063
SC-3	561	160	−20.9	0.84	9600 ± 150	0.00336
N-8	419	160	Not analyzed			
SC-4	419	160	−20.9	0.78	7120 ± 100	0.00249

Table 3
Laser concentration extrapolations. (a) Resulting extrapolated concentrations for the error-function fit to all laser data, disregarding the surface concentration measurement. (b) Resulting extrapolation from the Whipple–LeClaire fit to the laser data. (c) Measured surface concentrations from surface strip analyses (see text for discussion) for all samples with the 213 nm laser.

Sample	T (°C)	P (MPa)	Duration (h)	a (ppm)	b (ppm)	c (ppm)
N1	824	170	480	nm	nm	nm
N2A	764	170	480	50	190	91
N2B	764	170	480	0.6	x	
N2C	764	170	480	2.3	230	
N3	642	170	480	12	240	123
N4	489	170	480	9	150	74
N5	724	160	360	4	x	nm
SC-1	724	160	360	120	7350	3012
SC-E1	724	160	360	6000	6000	na
SC-E2	724	160	360	3300	9500	na
SC-E3	724	160	360	3000‡	x	na
SC-E4	724	160	360	530	1900	na
SC-E5	724	160	360	250	135	na
N6	669	160	360	nm	nm	na
SC-2	669	160	360	7	850	810
N7	561	160	360	–	–	–
SC-3	561	160	360	nm	nm	nm
N8	419	160	360	–	–	–
SC-4	419	160	360	nm	nm	nm

nm, not measured.
na, by 193 nm laser analysis only.
–, profiles measured but concentration information not extracted due to incomplete ablation of sample.
x, no appropriate fit could be made.
‡ Error-function fit to raw data only; see text.

where C is the concentration of argon (diffusing in), C_o is equivalent to the equilibrium solubility of argon in quartz (with respect to the pure pressurize argon gas medium), D is the diffusion coefficient ($m^2\ s^{-1}$), and t is the duration of the experiment run. The best fit provides both the relevant diffusivity and equilibrium surface concentration or apparent solubility (i.e., the maximum concentration extrapolated all the way to the surface of the crystal in equilibrium with its surroundings). All RBS profiles were modeled this way as the shape of the RBS diffusion profiles reveals a smooth error function form.

4.2. Modeling combined effects of two diffusion pathways: lattice and fast-path diffusion

In many of the profiles from the 213 nm and 193 nm UV-laser analysis, a significant kink, or break in slope was noted in the uptake profiles, separating higher concentrations in the outermost portion of the mineral, from lower concentrations deeper in (for example, Figs. 4b or d, 5a). With this sharp kink, a simple error-function diffusion model can not appropriately reproduce the entire profile and gives erroneous results; no error-function fits to raw laser data are reported. In other diffusion studies (Zhang

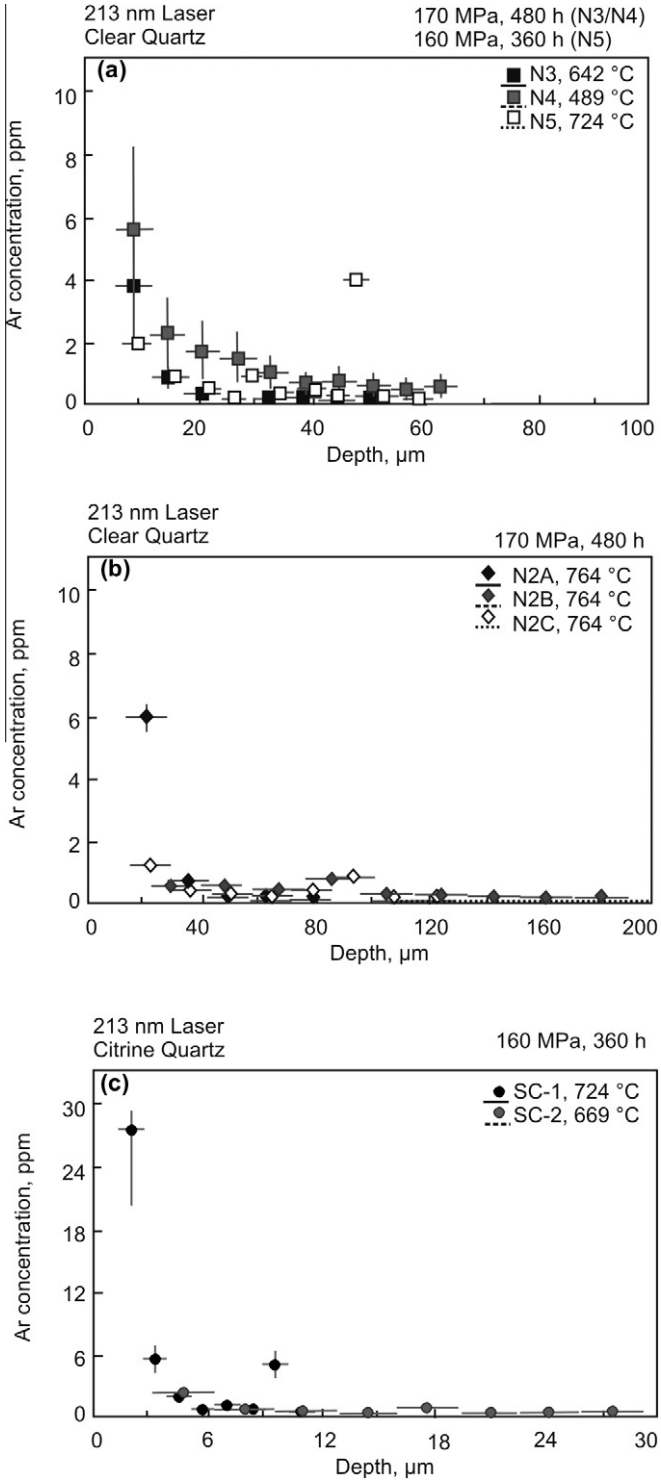

Fig. 3. UV-laser (213 nm) depth profiles in clear quartz. (a) All measured 213 nm laser argon concentrations (ppm) vs. depth (μm) profiles for natural quartz samples N3–N5 (expt. #1 and #2) fit to the error function (a). Repeat profiles for sample N2 (N2A–N2C) are shown separately in (b) due to differences in depth-scale. Citrine quartz profiles for samples SC-1 and SC-2 are shown in (c). Surface strip data, which were acquired for all profiles, are not shown on plots but all give concentrations between 74 and 123 ppm argon in the clear quartz and 810–3012 ppm argon in the citrine quartz (Table 3, column d). Symbols and experiment temperatures given on the plots.

et al., 2006), such a kink has been interpreted as evidence for a second diffusion mechanism other than volume lattice diffusion, which could be a significant mechanism for transport deeper into the mineral. In this scenario, the nearest surface data with high concentrations and relatively steep slope represent argon diffusing via the lattice, whereas

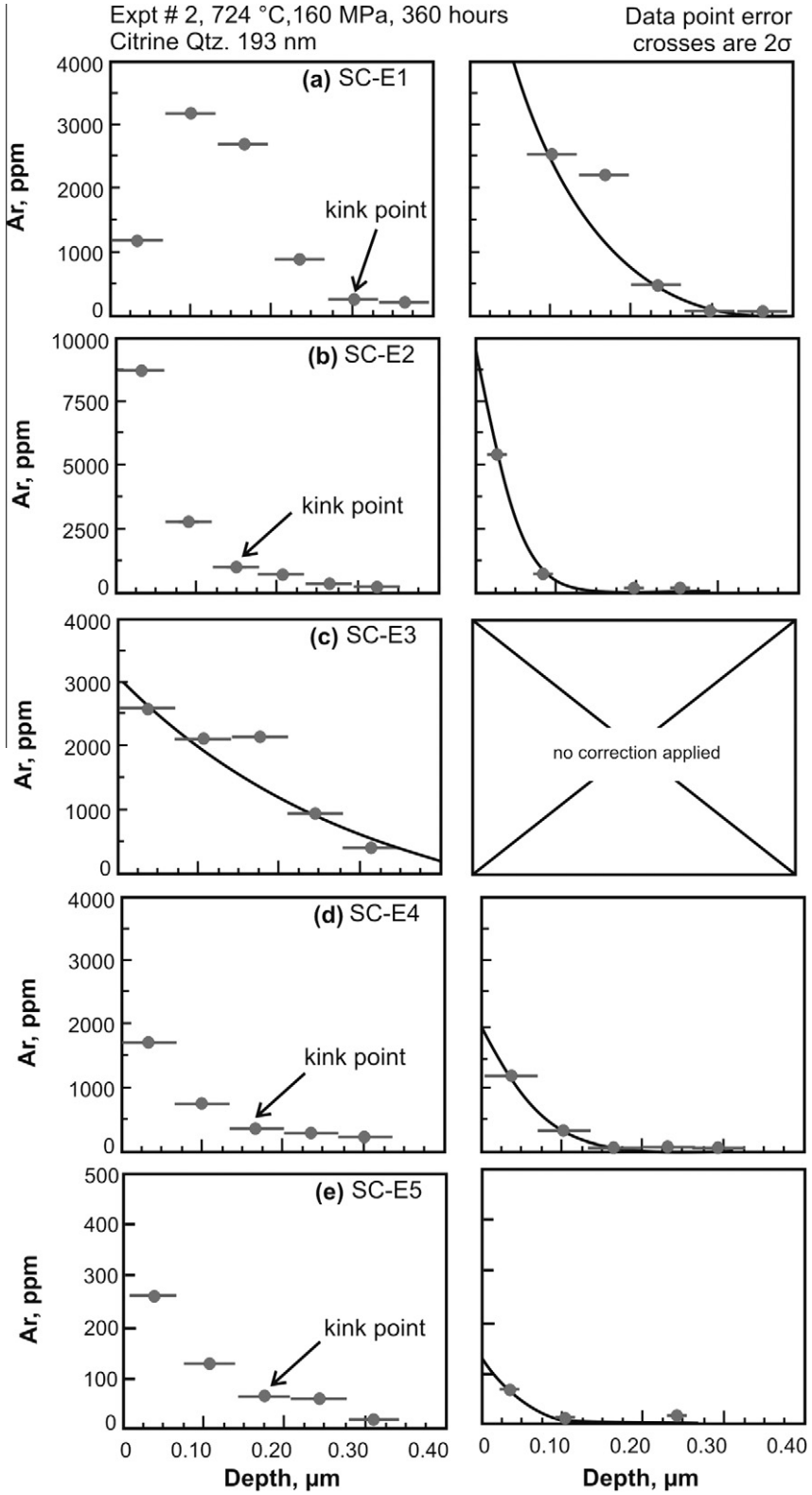

Fig. 4. The five depth (μm) vs. concentration (ppm) profiles on citrine sample SC-1 (profiles labeled SC-E1 to SC-E5) as measured by 193 nm laser. Profiles SC-E1, E2, E4, and E5 illustrate the raw data with the 'kink' point in the profile (left) and the Whipple–LeClaire corrected fit by subsequent modeling by the error-function (right) (R^2 given in Table 4). Profile SC-E3 (c) does not demonstrate any identifiable kink in the data shown in the left panel, and therefore the error-function fit to all data is given (see text for discussion).

deeper in the mineral, argon penetrates further via a "fast path" (Lee, 1995; Zhang et al., 2006). In a few of our analyses, the hypothesized effects of lattice diffusion appeared to penetrate beyond the very first surface strip layer in the 213 and 193 UV-laser profiles; that is, the "kink" in the profile occurs after the first two data points in a profile. In these cases where the hypothesized effects of the two pathways could be resolved and differentiated, an attempt was made to extract and separate the contributions from the lattice and fast-path following the method outlined by Zhang et al. (2006).

The Whipple–LeClaire equation (Whipple, 1954; LeClaire, 1963) has been used to describe fast diffusive transport via planar grain boundaries combined with the slower effects of lattice diffusion into the mineral from the grain boundaries themselves. It is used here as an approximation for the "fast diffusive pathways" present in quartz (which may or may not be planar features). The Whipple–LeClaire equation captures the net behavior of argon uptake and provides a first order means of quantifying the process. The equation is:

$$\delta D_b = 1.332\left(\frac{D}{t}\right)^{1/2}\left(-\partial \ln \bar{c}/\partial z^{6/5}\right)^{-5/3} \quad (2)$$

where δD_b is the product of the fast-path diffusivity and the width of the planar fast path feature. D is the lattice diffusion coefficient and δ is the thickness of the intracrystalline "fast paths" which may (in our samples) be pipes or planar defect feature, z is the depth, t is the experiment time and $\bar{c}$ is the average concentration that occurs in a slice that is perpendicular to the fast path.

The "two-path de-convolution" approach described above has practical value in quantifying our results, but it is worth noting there are other possible interpretations of "kinked" diffusion profiles. Use of the Whipple–LeClaire equation implicitly assumes that the steep, near-surface portion of the diffusive uptake profile represents a "normal" (slow) lattice diffusion and the shallow tail represents transport through an extended fast path. Indeed, this is one likely physical end-member to describe the data. If, however, the steep portion is taken to represent in-diffusing argon atoms trapped in natural isolated point defects (Watson et al., 2007; Thomas et al., 2008), then the diffusivity pertaining to this region must be viewed not as the diffusivity in a perfect lattice, but rather as an effective diffusivity representing the convolution of lattice diffusion with immobilization in local, isolated argon sinks. In this conceptualization, the argon concentrations in the near-surface become only apparent lattice solubilities – not the solubilities that would apply to a perfect defect-free crystal lattice. The interpretation of the argon tails in this case could change: they could indeed represent fast-path transport as we have assumed in our analysis, but it is also possible that they represent the few argon atoms diffusing through the lattice that have escaped defect trapping. Either way, however, the diffusivities we recovered from the experiments are useful for estimating the time- and length-scales appropriate to argon transport in natural quartz, especially insofar as virtually all natural quartz crystals in the dynamic crust will include defects.

5. RESULTS

5.1. RBS profiles: lattice diffusion

Diffusivities resulting from error-function fits to RBS data are listed in Table 2. Citrine and clear quartz exhibit similar diffusivities, though they show highly variable apparent solubilities, with the citrine quartz (7120–13,450 ppm) exhibiting higher concentrations than the clear quartz (1050–9750 ppm). The RBS apparent solubility data for each quartz sample analyzed is summarized in Table 2. In general, the natural quartz produced smoother profiles than the citrine quartz.

5.2. Laser profiles

5.2.1. Modeling laser depth profiles: 213 nm

When using the laser data to extract diffusivities, different model approaches can be taken: Ignoring the high surface concentrations and disregarding it as adsorbed argon on the mineral surface, whereby the rest of the profile is fit to a typical diffusion curve (given in Table 3 column a), or a composite fit including both slow lattice diffusion and "fast-path" diffusion using the Whipple–LeClaire equation can be made (Table 3 column b) (see Section 5.2.1.3 below). Alternatively, another approach can be taken whereby the incorporation of the high surface concentration is forced to an error-function fit of all the data, however, this approach is not attempted nor reported here.

5.2.1.1. Shallow diffusion profiles. In many previous studies of argon diffusion using UV-laser ablation (e.g., Wartho et al., 1999), nearest surface analyses appear to have unexpectedly, and inconsistently, elevated concentrations deviating significantly from the rest of the profile, as do several of the profiles illustrated in this study. Frequently, these elevated or "anomalous" surface points are disregarded because of the possibility they include significant adsorbed argon on (rather than in) the mineral surface. Following this approach, the main problem is choosing which (if any) data within the profile to discard as relicts of atmospheric surface adsorption, or other damage effects. There is a challenge in deciding how to model the 213 nm profile data because the surface strip data indicates much higher surface concentrations than deeper with the sample and cannot be fit appropriately by a forcing a single error-function fit to the profile. Discarding this surface strip point produces a reasonable fit to the rest of the data, giving the resulting apparent solubility given in Table 3 (column a) and diffusivity listed in Table 4 (column a). While there is considerable variability in concentration, the spatial resolution allows for an appropriate fit to all points of the sample.

The problem with this approach is illuminated when comparing the apparent solubility from this modeling of 213 nm laser ablation data to the apparent solubility from modeling of the RBS and 193 nm UV-laser ablation data; they differ by orders of magnitude. As described in greater detail in Section 3.1, the RBS data show a smooth and systematic diffusive uptake profile penetrating up to 250 nm

Table 4
Diffusion data obtained from laser analyses. (a) Calculated diffusion data for all minerals from 213 laser concentration-depth profiles excluding the surface concentration. (b) Calculated 213 and 193 nm laser diffusion data for all minerals using the Whipple–LeClaire fit to exclude the fast-path component and fitting the resultant data to the error-function. (c) Calculated δD_b for 213 and 193 nm laser diffusion profiles.

Sample	T (°C)	P (MPa)	Duration (h)	a, log D (m^2/s)	R^2	b log D (m^2/s)	R^2	c, δD_b (cm^3/s)
N1	824	170	480	–		–		nm
N2A	764	170	480	−16.3	0.58	−16.5	0.99	7.46×10^{-15}
N2B	764	170	480	−14.3	0.98	x		3.53×10^{-14}
N2C	764	170	480	−15.5	0.51	−16.7	0.99	2.18×10^{-14}
N3	642	170	480	−16.7	0.99	−17.3	0.98	9.94×10^{-15}
N4	489	170	480	−17.0	0.92	−17.3	0.98	1.32×10^{-14}
N5	724	160	360	−16.2	0.10	x		x
SC-1	724	160	360	−18.1	0.97	x	0.98	2.2×10^{-15}
SC-E1	724	160	360	na		−20.2	0.95	1.8×10^{-16}
SC-E2	724	160	360	na		−21.0	0.95	9.10×10^{-17}
SC-E3	724	160	360	na		−19.7‡	0.88	x
SC-E4	724	160	360	na		−20.7	0.95	3.1×10^{-16}
SC-E5	724	160	360	na		−21.0	0.84	1.2×10^{-16}
N6	669	160	360	na		na		na
SC-2	669	160	360	−17.0	0.87	−21.0	0.99	9.33×10^{-15}
N7	561	160	360	na		na		na
SC-3	561	160	360	na		na		na
N8	419	160	360	na		na		na
SC-4	419	160	360	na		na		na

nm, not measured.
na, by 193 nm laser analysis only.
–, profiles measured but concentration information not extracted due to incomplete ablation of sample.
x, no appropriate fit could be made.
‡ Error-function fit to raw data only; see text.

into the quartz lattice and are thus internally consistent. On this basis, we do not believe that ignoring the near surface laser layers is the correct way to model and describe the laser data. Rather, it appears that the high near surface concentrations as measured by UV-laser should not be discarded as they are consistent (at least within an order-of-magnitude) with the RBS data and shallow 193 nm laser depth profiles.

5.2.1.2. Adsorption of argon? The adsorption of argon is often cited as a potential complication for studies where argon solubilities were regarded as too high (e.g., studies utilizing mineral powders; Broadhurst et al., 1990, 1992; Shiabata et al., 1994) and contaminating argon on mineral surfaces has been suggested to have affected such studies (Roselieb et al., 1997; Brooker et al., 1998; Chamorro et al., 2002). Several studies (Brooker et al., 1998; Wartho et al., 1999; Heber et al., 2007) also attributed high surface concentrations in the outermost surface layers of polished mineral surfaces (1–6 nm) to contaminating adsorbed argon. However, recent investigation (Thomas et al., 2008) led to several 'zero-time' experiments involving the pressurization of minerals in Argas without heating and experiments in air following typical in-diffusion procedure, but holding at temperature for very short durations (min) to determine if the presence of adsorbed argon could be detected. Neither of the zero-time experiments revealed any measurable surface argon, demonstrating that adsorbed argon, if present, is a transient phenomenon that will not affect diffusion profiles. The findings of Thomas et al. (2008) confirm that studies involving high temperature, long-duration experiments will not be compromised by any adsorbed surface contamination of argon.

5.2.1.3. Whipple–LeClaire profile fits. Following Zhang et al. (2006), fitting the data to isolate the two contributions (lattice and fast path) is done in several parts (see Fig. 5 for an example of the Whipple–LeClaire fitting procedure on an argon diffusion profile in citrine quartz): (1) On a plot of ln C vs. $x^{6/5}$ (where C is concentration) the highest concentration that can be attributed to the fast path is selected (i.e., the kink or separation point between what should be two roughly linear relationships with different slopes, typically the first 1–2 surface points), (2) a straight line segment is drawn from the origin to that highest concentration point to approximate the fast-path contribution in the near surface region where it overlaps with surface-perpendicular lattice diffusion, (3) the fast-path contribution is subtracted from the data to leave only the surface-perpendicular lattice diffusion contribution. The resulting profile (which may be only 2–3 significant points nearest the surface in this study) can then be fit using the error-function curve (Eq. (1)), and the resulting lattice diffusivity can be extracted. Once this lattice diffusivity (D) is determined, the Whipple–LeClaire equation can be used to quantify the δD_b of the fast paths.

If we accept that the near surface laser data represent slow diffusion of argon into the quartz lattice, we must call upon a different mechanism for the argon measured in laser ablation analyses deeper within the sample. There is a sharp kink between the shallow profile measured using RBS and

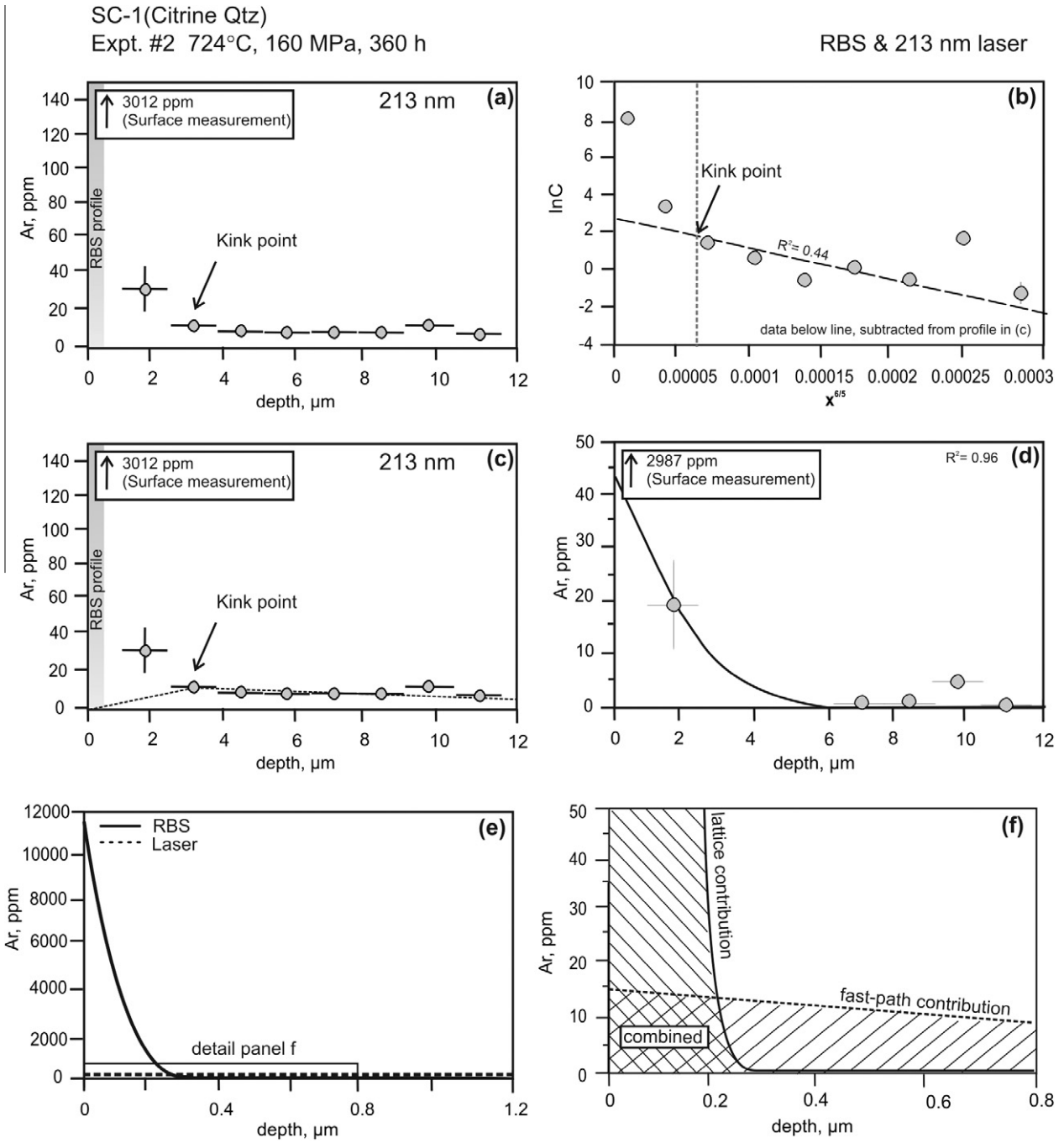

Fig. 5. (a) 213 nm laser measured diffusion profile from citrine sample SC-1 at 724 °C. Note the high surface concentration point (surface strip measurement at 3012 ppm argon, not illustrated on the plot due to scale differences), which makes a fit to the error-function problematic. For comparison, the range represented by a typical RBS profile (as seen in Fig. 2) is shown by a shaded grey bar next to the axis. (b) Plot of ln C vs. depth$^{6/5}$, showing the fit of the line (note the kink point in the curve). The second-to-last data point was discarded as an outlier as it was anomalously high compared to its neighbors. The equation of the line shown is used to calculate the contribution by the fast-path from the Whipple–LeClaire formulation. The fit of the fast-path contribution linear segment is shown in the original profile in (c). The dashed line shown in the left panel represent the Whipple–LeClaire linear approximation of the fast-path contribution translated into depth (μm) vs. concentration (ppm) coordinates. The linear segment from the kink point to the origin shows the overall fast-path contribution. The Whipple–LeClaire corrected profile is shown in (d). This profile is then fit to the error-function (R^2 given) (e) Modeled contribution of the lattice diffusion (solid black line) and fast path (dotted black line), with a close up of the overlapping components in (f). The cross hatched portions represent the separate contributions of each pathway, showing the area of overlap.

193 nm laser ablation (including the nearest surface laser layers) and the deeply penetrating 213 nm laser data. In some cases, this kink point is apparent beyond the first surface layer of laser analyses. In this case, the more deeply penetrating, lower concentration laser data can be described by a model of fast-path diffusion as outlined in Section 5.2.1.3. Note that the second laser-derived data point from the diffusion profile of sample SC-1 (Fig. 5a) is slightly, though significantly, elevated above the trend suggested by the rest of the profile, reflecting the influence of higher concentrations from a slower diffusive pathway.

In this case, a fit ignoring the surface data point and the second data point could be made. Such a fit, with results listed in Table 3 (column b), would be analogous to diffusive uptake via the "fast-path" and can be modeled using the Whipple–LeClaire equation (Eq. (2)) for an appropriate fit. However, especially in the case of the clear quartz, the kink point is not always obvious, and with the highly variable profiles, a reasonable fit can be difficult to make. The resulting diffusivities from the error-function fit to the Whipple–LeClaire modified profile are listed in Table 4 (column b). Calculated δD_b values are listed in column "c" of Table 4.

5.2.2. Modeling laser depth profiles: 193 nm

Fig. 4 details the profiles resulting from 193 nm analyses. The range in concentrations-depth data is shown (left) and the error-function fit to Whipple–LeClaire corrected data (right). These profiles exemplify the variability in the argon concentrations seen in citrine quartz. Profiles SC-E2, SC-E4, and SC-E5 (Fig. 4b, d, e) nicely illustrate the kink point, or break in slope, in the diffusion profile. Profile SC-E1 also appears to show a kink, though slightly deeper into the mineral. The low concentration in the nearest surface point of profile SC-E1 is clearly anomalous – it is inconsistent with our in-diffusion experiments and all other measurements – and is thus ignored in our modeling. Profiles E1, E2, E4, E5 are all modeled as "two-pathway profiles" as described above (see Section 5.2.1.3). The resulting log D from the Whipple–LeClaire corrected data (right panels of Fig. 4) for SC-E1, E2, E4, E5 is given in Table 4 (column b) and calculated δD_b values are listed in column "c" of Table 4. Profile SC-E3 shows similar concentrations and similar depth of penetration as the other four profiles. However, it does not show a clear kink, or break in slope, in the profile. Thus, while we expect that the effects of a fast pathway probably do contribute to profile SC-E3 as in the others, for this profile only we simply perform an error-function fit to the raw data rather than attempting to arbitrarily subtract away a "fast path" contribution. Overall, this makes little significant difference in the lattice diffusivity calculated.

6. DISCUSSION

6.1. Sample preparation and the near surface crystal structure

6.1.1. Mineral surface structure

In the present study, we observe shallow, slow diffusion corresponding to high argon concentrations (and thus higher solubility) and faster, deeper diffusion corresponding to lower argon concentrations (and thus lower solubility). We have considered to what degree the surface structure of quartz may be significant in applying interpretations to the data set presented here. The surfaces of minerals are thought to be different than the bulk structure, both chemically and electronically, due to the termination of long range bulk structure at the mineral surface. The termination of the bulk lattice structure at the mineral surface results in a surface that, while related to the bulk lattice, is different energetically (Coyne and McKeever, 1990). α-Quartz surface structure has been investigated in several studies (e.g., DeLeeuw et al., 1999; Steurer et al., 2007) and the surface terminations have been shown to result in a 'dense' surface, (resulting from a surface with three-times as many oxygen atoms and subsequent layer with two-times as many Si-atoms as a normal cleaved quartz surface; Steurer et al., 2007). Whilst it could be envisaged that such a 'dense' or otherwise anomalous surface structure could perhaps explain the slow diffusion observed in the outer few hundred nanometers in the quartz crystals we have studied, this structure does not extend deep enough into the crystal (no more than a few monolayers, or a few nanometers; e.g., Thomas et al., 2008, see below) to lend an explanation for the different diffusive regimes observed in the present study. Conversely, a defect-rich structure would be required for enhanced incorporation of argon atoms into the quartz lattice to explain the high argon concentrations. In contrast, Du et al. (2008) modeled the solubility of noble gases in a mineral lattice and at the surface, showing that heavier noble gases (they used the extreme example of Xe in MgO), had lower solution energies at the surface than in the lattice, whereas the lighter noble gases did not show the same disparity. Du et al. (2008) argued that the apparently higher solubility of heavy noble gases seen in some experiments might be the result of this surface enrichment of noble gases. We were unable to test this hypothesis since only argon was analyzed during the present study.

Thomas et al. (2008) suggested that the movement of argon atoms into a crystalline lattice which contains a number of vacancies can be envisaged as being slowly filled with argon as it moves into the crystal from an external argon pressure during the course of an experiment and further speculated on the potential role of point defects on argon solubility in minerals. Thomas et al. (2008) also suggested that evidence for higher argon solubility in Fe-bearing minerals over Fe-free phases might indicate a defect-related solution mechanism caused by an increase in thedefect population of a given phase with the progressive oxidation of Fe^{2+}. The present work also detected higher argon concentrations in citrine than the clear, Fe-free natural quartz.

6.1.2. Sample preparation and structural anomalies

Several studies have discussed the structure of the near-surface regions of the crystal lattice in the context of noble gas experiments (Roselieb et al., 1997; Wartho et al., 2005; Heber et al., 2007) and some have suggested that the near surface region of crystals are structurally anomalous compared to the interior mineral lattice. The implication of this hypothesis is that high apparent solubilities are an artifact

of such a structurally anomalous surface layer, and are not representative of the bulk crystal lattice. However, in addition, several studies have carefully characterized the near-surface structure of minerals (e.g., calcite, barite, orthoclase, quartz, enstatite, forsterite; Fenter et al., 2000, 2001; Schlegel et al., 2002; Watson and Cherniak, 2003; Thomas et al., 2008) by various means. The study of Thomas et al. (2008) demonstrated through the use of electron backscatter diffraction (EBSD) that pre-annealed and the essentially perfect crystalline surfaces of colloidal-silica polished samples do not differ from natural crystal faces, and revealed that the outer 10 nm of the crystal lattice is structurally indistinguishable to the interior. From this study, Thomas et al. (2008) were able to conclude that the notorious damaged 'Beilby' layer, of measurable thickness, oft discussed in experimental studies did not exist in their samples, including in un-polished natural facets. Other studies (Fenter et al., 2000, 2001) document the presence of a structurally anomalous layer, though this layer is restricted to only the first 1–2 nm, after which the structure is identical to the interior lattice. Particularly for quartz, this layer has been quantified to extend no more than 1.4 nm into the quartz lattice (Schlegel et al., 2002). The suggestion that increased argon uptake could occur through networks of fractures and dislocations induced through mechanical polishing in the near surface is not corroborated by the data in this study. Instead, we see *low* diffusivities in the outermost ~100 nm of the crystal, not the high diffusivities that would occur through enhanced diffusion anticipated if such a defect-rich, structurally anomalous layer were present. The consistency of the diffusion data extracted from quartz samples in this study with that of Watson and Cherniak (2003), using a combination of pre-annealed, colloidal silica-polished (0.06 μm) and natural crystal faces, is further testament that we are observing lattice diffusion rather than a simple phenomenon due to the presence of a structurally anomalous defect-rich layer, with enhanced argon incorporation and diffusion in a Beilby layer induced by mechanical polishing.

6.2. Diffusion data: lattice versus fast path

Consistent with previous work by Watson and Cherniak (2003), we see a very smooth, well-behaved diffusive profile for quartz with respect to RBS and 193 nm laser ablation analysis and depth-scale (on the order-of-~100–250 nm to 400 nm, respectively). Data are well fit by an error-function fit to the diffusion profiles (Eq. (1)). The diffusion data obtained from RBS profiles for both quartz samples is plotted on an Arrhenius diagram (Fig. 6). As shown in Fig. 6, our data are in good agreement with the previous work of Watson and Cherniak (2003) and Thomas et al. (2008). Importantly, both the RBS and the 193 nm laser measured lattice diffusivities produce consistent results.

Argon concentrations observed in the diffusion profiles reveal a general increase of concentration towards the surface of the quartz surface. However, occasional jumps or spikes in concentration with depth in the crystal were observed; this was seen most obviously in the clear quartz, but also in the citrine quartz to a lesser degree. These argon

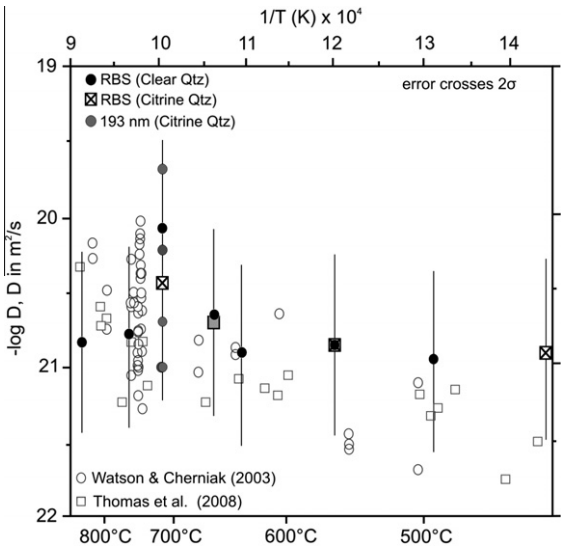

Fig. 6. Summary of diffusion data for combined RBS (clear quartz represented as black circles and citrine quartz by white squares with black crosses) and 193 nm laser-derived data (grey circles) on an Arrhenius diagram ($1/T(\mathrm{K}) \times 10^4$ vs. $-\log D$ m^2/s). RBS clear quartz data from Watson and Cherniak (2003) and Thomas et al. (2008) are represented by the pale grey outlined open circles and pale grey outlined open squares, respectively.

concentration spikes are similar to those observed by Wartho et al. (2005) and probably relate to liberation of argon from micro fluid inclusions or defects in the crystal.

6.3. Area-normalized argon concentrations

With both the clear quartz and in particular the citrine quartz, we see a high capacity for argon manifested in the nearest surface few hundred nanometers, with concentration reaching thousands of ppm. This concentration drops off dramatically with depth, with subsequent data points showing concentrations less than 1 ppm. This is seen in both the RBS and 193 nm laser ablation analysis, but also in the surface analyses using the 213 nm UV-laser (Fig. 7). With regards to the concentrations of argon in the outermost surface layer, surface concentrations integrated over the outermost 200 nm of quartz were calculated to investigate apparent differences in measured surface concentrations between 213 nm, 193 nm laser analyses and RBS analyses. This analysis is necessary to make such comparisons given the order-of-magnitude difference in depth resolution of the three methods. Table 5 gives the calculated ranges for analyzed samples (in argon atoms in outermost 200 nm per area), illustrating that the values determined by 193 nm laser analyses lie within a similar range to the RBS determined concentrations (see also Fig. 7 for variations with temperature). There appears to be some discrepancy between the argon atoms per area determined by 213 nm-, 193 nm-laser analyses and RBS determined concentrations although range of determined concentrations overlap and the 213 nm analyses are punctuated by higher concentrations, seen especially in the two citrine analyses (Fig. 7a). The RBS analyses average much larger areas so

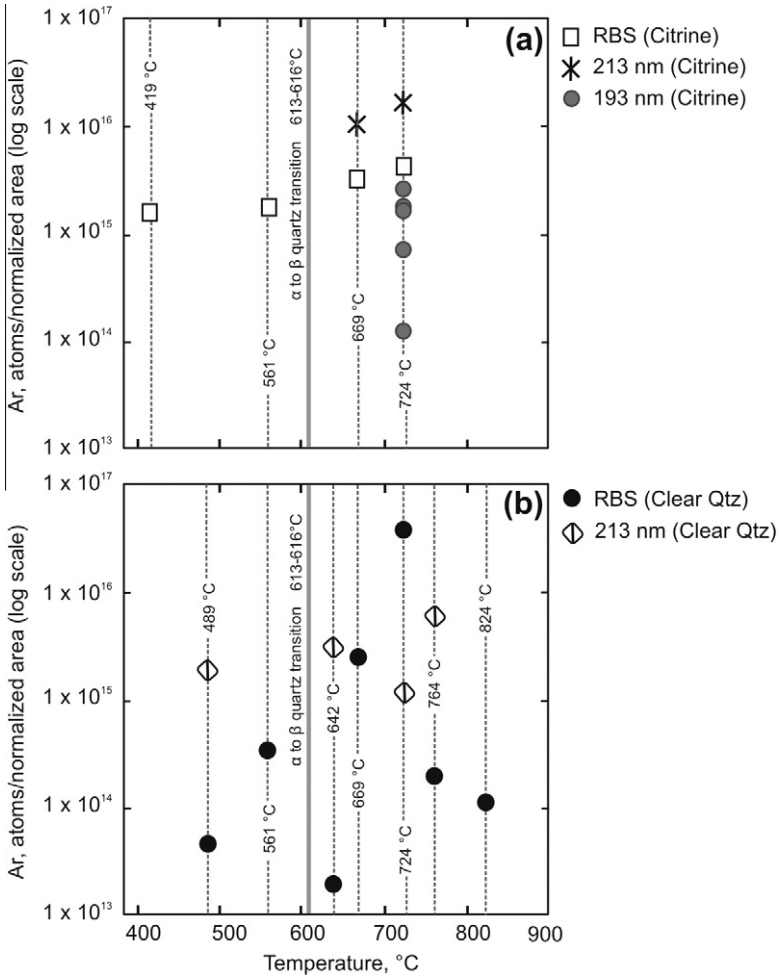

Fig. 7. Calculated normalized surface concentration (Ar atoms/area) variations (log scale) with temperature for RBS, 213 nm laser and 193 nm laser data on citrine (a) and clear (b) quartz. See text for discussion of the calculations. The temperature of each experiment is given by a dashed line, and the α-quartz → β-quartz transition for this experiment is given at 613–615 °C, represented by the narrow grey bar. Calculation of the transition based on occurrence at 573 °C, with an increase in 1 °C per 40 bar (expt. # 1 and # 2 are at 1700 and 1600 bar, respectively).

it is possible that the laser profiles (both 193 and 213 nm) reveal some heterogeneity in concentration across the mineral surface, particularly the citrine quartz which proved to be highly variable with regards to argon concentrations. This may in turn be due to the presence of trace Fe, which has been suggested to cause enhanced uptake of argon in Fe-bearing minerals (Thomas et al., 2008).

It should also be noted that for the temperatures and pressures that our experiments were conducted, the transition between α-quartz to β-quartz is anticipated. This occurs at 573 °C, but increases 1 °C for each 40 bar, giving an approximate temperature of 615 °C for experiment #1 (1700 bar; samples N1–N4) and 613 °C for experiment #2 (1600 bar; samples N5–8; SC-1 to SC-4).This is an instantaneous, displacive transition whereby only changes in the angles and lengths of Si–O bonds occur in the change from trigonal to hexagonal symmetry. While not a major structural change, there is a change in density from approximately 2.65 to 2.53 g/cm^3 which could result in a slightly more 'open' structure, suitable for accommodating more argon. The changes in calculated argon concentrations/area for each sample seen after this temperature (Fig. 7) are relatively minor, though there is a general increase towards higher concentrations of argon which may be the result of further accommodation of argon after this transition.

6.4. Significance of multiple diffusion regimes

On the basis of these experiments we propose a hypothesis of two separate diffusion pathways (illustrated in Fig. 8): (1) Lattice diffusion and (2) fast-path diffusion. The measurements made in this study provide evidence for these two distinct diffusion pathways, each operating throughout the crystal with its own rate of diffusion, geometry and contributions to the net diffusive uptake of argon. It seems likely that the different length-scales achieved by RBS (and 193 nm laser ablation) compared to the 213 nm UV-laser ablation, reveal these two different diffusion mechanisms.

Table 5
Area-normalized argon surface concentrations in quartz for (a) RBS, (b) laser-determined concentrations and (c) 193 nm laser-determined concentrations for sample SC-1.

Sample	T (°C)	P (MPa)	Duration (h)	(a) RBS	(b) 213 laser	(c) 193 laser
N1	824	170	480	1.1×10^{14}	nm	nm
N2	764	170	480	1.9×10^{14}	5.8×10^{15}	nm
N3	642	170	480	1.9×10^{13}	3.1×10^{15}	nm
N4	489	170	480	4.6×10^{13}	1.8×10^{15}	nm
N5	724	170	480	3.7×10^{16}	1.2×10^{15}	nm
SC-1	724	160	360	3.9×10^{15}	1.7×10^{16}	nm
SC-E1	724	160	360	193 only	193 only	1.8×10^{15}
SC-E2	724	160	360	193 only	193 only	2.7×10^{15}
SC-E3	724	160	360	193 only	193 only	1.8×10^{15}
SC-E4	724	160	360	193 only	193 only	7.3×10^{15}
SC-E5	724	160	360	193 only	193 only	1.2×10^{14}
N6	669	160	360	2.5×10^{15}	nm	nm
SC-2	669	160	360	3.1×10^{15}	1.0×10^{16}	nm
N7	561	160	360	3.3×10^{14}	nm	nm
SC-3	561	160	360	1.7×10^{15}	nm	nm
N8	419	160	360	nm	nm	nm
SC-4	419	160	360	1.5×10^{15}	nm	nm

nm, not measured.

In the laboratory experiments, lattice diffusion is slower and thus occurs over shorter length-scales (~10's to 100's of nm for our experimental timescales; Fig. 8a and b). These are extremely significant concentrations on the order of thousands of ppm but the depth to which these high concentrations of gases penetrate is extremely shallow over the short duration of the experiments. If these high concentrations reflect the true intrinsic lattice solubility, then that value can be compared to solubilities in other phases in order to calculate equilibrium partitioning coefficients (cf. Watson et al., 2007). However, given the very slow lattice diffusivity, it is pertinent to consider how long it will take for quartz to reach these high equilibrium concentrations, especially as virtually all of the radiogenic ^{40}Ar that might accumulate in quartz must diffuse in from external K-bearing sources of fluids in the intergranular transporting medium/grain boundary network.

6.4.1. Quartz as a sink for argon?

The existence of multiple paths for diffusion has significance for geochronology (closure temperature models), models for evolution of terrestrial degassing, rates of argon uptake/loss, and models for the presence and transport of excess argon in various geologic systems. Multi-path diffusion affects how we model diffusive uptake or release of argon from quartz. For example, as fast paths are generated and become more concentrated or abundant (i.e., due to progressive deformation) a net effect is to decrease the effective diffusion length-scales for lattice diffusion, thus also decreasing the timescale to fill the quartz lattice up to the potential lattice solubility. This can be important for shorter-lived systems (e.g., magmatic or volcanic timescales).

The fast-paths are significant in determining the relative ability of quartz to act as a sink for noble gases in various geologic systems (see Fig. 9). For example, despite high lattice solubilities, quartz will not be an important sink for argon in magmatic systems, due to the short timescales involved (~1 Ma). While the capacity for argon is high, there is not enough time in such systems for the solubility limit to be effectively reached. However, we stress again that the actual solubility would rarely be reached given natural argon concentrations; it is the relative solubility (i.e., partitioning) between different available phases that determines the equilibrium distribution of argon. Still, in this regard, the sluggish diffusivity of the high solubility quartz lattice significantly decreases its ability to act as an effective sink with respect to other mineral and fluid phases (cf. Baxter, 2003) except in very long-lived systems. Fast-paths may act to move argon into the lattice over shorter durations, though never approaching equilibrium concentrations. Even though significant uptake of argon into quartz would not occur over magmatic timescales, any shallow uptake (or loss) profiles in quartz could then be used as a measure of magmatic or eruptive timescales.

6.4.2. Physical nature of the fast paths

The use of the Whipple–LeClaire model to describe the deeper diffusion and fast-paths provides a useful end-member conceptual and quantitative description of the phenomena. However, the approximation of the fast paths as planar features is made based on similarity with earlier experiments (Zhang et al., 2006) and not on the basis of direct physical observations from the present work. Similar experiments in other minerals with higher argon concentrations may provide solution to this problem. Fast-path diffusion, as measured in the present experiments, is not lattice-controlled (though argon having deeply penetrated a mineral via fast-paths may then begin to diffuse slowly into the lattice at depth) but instead is presumably dominated by extended defects, dislocations, or planar features in the mineral. It carries much lower concentrations of argon (only on the order of 1 ppm, compared to 1000's of ppm for lattice diffusion) but it appears to transport these gases faster and deeper into the crystal lattice, penetrating

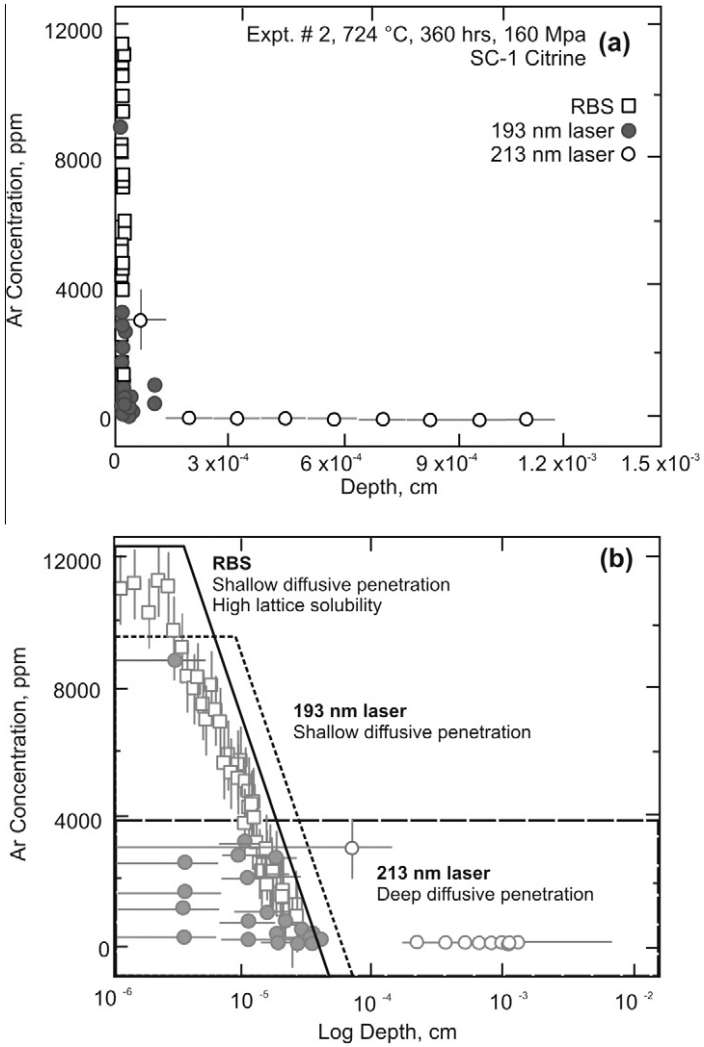

Fig. 8. Compilation plot of RBS, 213 nm- and 193 nm-laser data for synthetic citrine. The concentration (ppm argon) vs. depth (cm) is given linearly (a) and also in log-depth-scale (b) due to the vast differences in depth-scales of each technique. RBS points represented by an open square, 213 nm-laser points by and open circle and 193 nm-laser points by a grey circle. The contribution (concentration and depth) of each path is outlined in (b): RBS profile encapsulated by a solid black line, 193 nm laser data by the short-dash line and the 213 nm data by the long-dash line.

to 100's of microns over the duration of our experiments. The transport capacity of each path is determined by its width, and partitioning of argon between the fast path, the intergranular transporting medium and the mineral lattice. All of this is encapsulated in the δD_b term (of Eq. (2)) and controls how well argon can be brought deeper in to the quartz before it can start diffusing out of the fast path and into the lattice.

It is difficult to speculate on the physical nature and properties of the fast-paths that result in drastically different diffusivities. Fractures, dislocations and extended crystal defects (e.g., micro-structural defects, edge/screw dislocations, micro-fractures) would all have potential to create such enhanced diffusion pathways. Greater physical characterization of potential fast-paths in mineral phases would allow for increased understanding of their overall impact on the apparent solubility of argon in minerals, and how such a contribution can be identified. One of the main concerns is the size, density, anisotropy and interconnectivity of such paths. These parameters will ultimately affect the contribution the fast paths will have on the overall diffusivity, and whether or not the two distinct diffusion pathways can be appropriately decoupled. Moreover, Watson and Cherniak (2003) describe the existence of "nanopores" in quartz samples from 70 nm down to the 10–15 nm pore size range which can be seen in SEM images. Differences in densities of these nanopores may also provide support for the general scatter present in the surface concentrations observed, particularly if present in the hydrothermally, synthetically synthesized citrine quartz. As noted earlier, the existence of "nanopores" or isolated defects throughout the crystal could possibly contribute to the high apparent lattice solubility and slow apparent lattice diffusivity in the outermost ~200 nm where such features could be acting a mini sinks for argon, retarding net diffusive transport. In this conceptualization, then as the

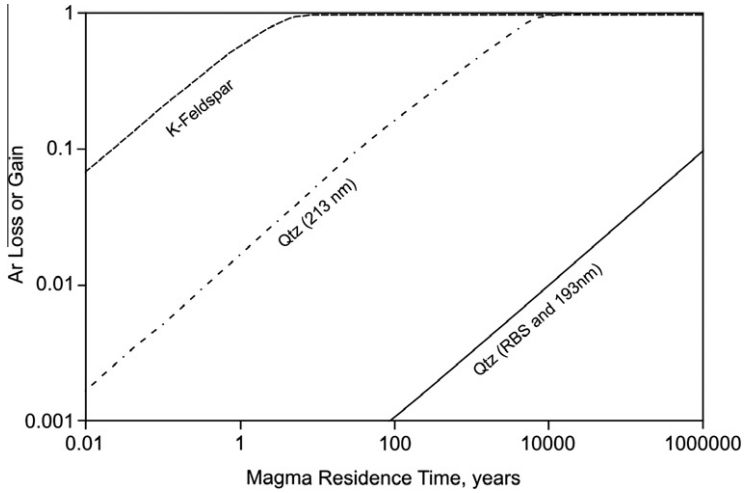

Fig. 9. Relative loss or gain of argon over magmatic timescales for K-feldspar (dashed line; using diffusion data from Wartho et al., 1999), quartz using RBS and 193 nm laser determined diffusion parameters (calculated at 700 °C from this study; black line) and a "fast-path" equivalent, using diffusion parameters derived from a 213 nm laser (grey line; data from this study). Loss/gain modeled for a spherical geometry.

density of such isolated nanopores or defects varies in natural samples, so too will the effective lattice solubility and diffusivity.

7. SUMMARY

Analysis of a single sample using both UV-laser ablation and RBS techniques has allowed us to identify two different diffusive regimes in clear, natural rock crystal quartz and synthetic citrine quartz. This study's laser ablation data set confirms very slow lattice diffusion for argon in quartz previously observed from RBS measurements alone (Watson and Cherniak, 2003; Thomas et al., 2008). This slow lattice diffusion in quartz would be overlooked with the sole use of 213 nm UV-laser ablation or even spatially coarser analytical tools. In some previous work, high concentrations in the surface layers of UV-laser depth profiles has been discarded as "anomalous" argon (e.g., Wartho et al., 1999). In the case of quartz, this shallow nearest surface profile appears to represent the lattice diffusion and solubility (though perhaps including the effects of natural isolated defects) and should not be ignored.

The 193 nm laser yields fine enough spatial resolution to capture and reproduce the RBS lattice diffusion for argon in quartz. Both methods of analysis produce meaningful and consistent results; the only difference is in the scale and resolution of observation (RBS analysis produces many tens of data points within 0.1 μm, whereas 193 nm laser analyses produce 1–2 data points in the same 0.1 μm).

The existence of fast diffusion pathways has been observed in the deeper diffusive profiles measured by 213 nm laser ablation. If the high concentration seen in the lattice represents the lattice solubility and diffusivity, then the deeper portions of laser analysis represent the effect of the fast-path diffusivity. This observation raises the issue for other UV-laser ablation measured profiles such as that measured in K-feldspar (e.g., Wartho et al., 1999). While the Wartho et al. (1999) measurements are real and valid, they have been interpreted in the past as lattice diffusivity and the implication from the present experiments may be that they, and other geochronologically important argon diffusion measurements, may represent fast-path diffusion. As discussed above, the fast paths are no less important in controlling the manner in which argon enters (or exits) a crystal, but the mathematical treatment of multi-path diffusion is fundamentally different and may need to be considered in many minerals.

ACKNOWLEDGMENTS

We are grateful to Jon Price for help in setting up experimental work. James Schwanethal is thanked for assistance with laser analyses and Richard Chater, Imperial College London, is thanked for help with laser-pit depth measurements. Constructive comments and suggestions from Steve Parman and two anonymous reviewers improved the manuscript significantly. We also thank B. Mysen for thoughtful and constructive editorial handling. This work was funded by NSF Grant # EAR-0337527 awarded to E.F.B and aspects of this work conducted at RPI were supported by NSF Grant # EAR-0738843 awarded to E.B.W.

APPENDIX A. SUPPLEMENTARY DATA

Supplementary data associated with this article can be found, in the online version, at doi:10.1016/j.gca. 2010. 07.014.

REFERENCES

Arnaud N. O. and Kelley S. P. (1995) Evidence for widespread excess argon during high pressure metamorphism in the Dora Maira (Western Alps, Italy), using an ultra-violet laser ablation microprobe $^{40}Ar/^{39}Ar$ technique. *Contrib. Mineral. Petrol.* **121**, 1–11.

Balluffi R. W. (1970) On measurements of self-diffusion rates along dislocations in FCC metals. *Phys. Status Solidi* **42**, 11–34.

Baxter E. F., DePaolo D. J. and Renne P. R. (2002) Spatially correlated anomalous Ar-40/39Ar "age" variations in biotites about a lithologic contact near Simplon Pass, Switzerland: a mechanistic explanation for excess Ar. *Geochim. Cosmochim. Acta* **66**(6), 1067–1083.

Baxter E. F. (2003) Quantification of the factors controlling the presence of excess ^{40}Ar or ^{4}He. *Earth Planet. Sci. Lett.* **216**, 619–634.

Broadhurst C. L., Drake M. J., Hagee B. E. and Bernatowicz T. J. (1990) Solubility and partitioning of Ar in anorthite, diopside, forsterite, spinel, and synthetic basalt. *Geochim. Cosmochim. Acta* **54**, 299–309.

Broadhurst C. L., Drake M. J., Hagee B. E. and Bernatowicz T. J. (1992) Solubility and partitioning of Ne, Ar, Kr, and Xe in minerals and synthetic basaltic melts. *Geochim. Cosmochim. Acta* **56**, 709–723.

Brooker R. A., Wartho J.-A., Carroll M. R., Kelley S. P. and Draper D. S. (1998) Preliminary UVLAMP determinations of argon partition coefficients for olivine and clinopyroxene grown from silicate melts. *Chem. Geol.* **147**, 185–723.

Chamorro E. M., Brooker R. A., Wartho J. A., Wood B. J., Kelley S. P. and Blundy J. D. (2002) Ar and K partitioning between clinopyroxene and silicate melt to 8 GPa. *Geochim. Cosmochim. Acta* **66**, 507–519.

Coyne L. M. and McKeever W. S. (1990) Spectroscopic characterization of minerals and their surfaces. In *Spectroscopic Characterization of Minerals and Their Surfaces* (ed. L. Coyne). American Chemical Society, Washington, DC.

Crank J. (1975) *The Mathematics of Diffusion*, second ed. , 414pp.

de Jong K., Wijbrans J. R. and Feraud G. (1992) Repeated thermal resetting of phengites in the Mulhacen Complex (Betic Zone, southern Spain) shown by ^{40}Ar–^{39}Ar step-heating and single grain laser-probe dating. *Earth Planet. Sci. Lett.* **110**, 173–191.

DeLeeuw N. H., Higgins F. M. and Parker S. C. (1999) Modeling the surface structure and stability of α-quartz. *J. Phys. Chem. B* **103**, 1270–1277.

Dohmen R., Chakraborty S. and Becker H.-W. (2002) Si and O diffusion in Fe-bearing olivine and implications for characterizing plastic flow in the mantle. *Geophys. Res. Lett.* **29**(21), 26-1–26-4.

Du Z., Allan N. L., Blundy J. D., Purton J. A. and Brooker R. A. (2008) Atomistic simulation of the mechanisms of noble gas incorporation in minerals. *Geochim. Cosmochim. Acta* **72**, 554–573.

Fenter P., McBride M. T., Srajer G., Sturchio N. C. and Bosbach D. (2001) Structure of barite (1 0 0)– and (2 1 0)–water interfaces. *J. Phys. Chem.* **B105**, 8112–8119.

Fenter P., Teng H., Geissbuhler P., Nagy K. and Sturchio N. C. (2000) Atomic scale structure of orthoclase (0 0 1)–water interfaces measured with X-ray reflectivity. *Geochim. Cosmochim. Acta* **64**, 3663–3673.

Foland K. A. (1974) 40Ar diffusion in homogeneous orthoclase and an interpretation of Ar diffusion in K-feldspar. *Geochim. Cosmochim. Acta* **38**, 151–166.

Giletti B. J. (1974) Studies in diffusion I: argon in phlogopite mica. In *Geochemical Transport and Kinetics* (ed. A. W. Hoffman et al.). Carnegie Inst. Wash. Publ. 634, pp. 107–115.

Gilleti B. J. and Tullis J. (1977) Studies in diffusion IV: pressure dependence of Ar diffusion in phlogopite mica. *Earth Planet. Sci. Lett.* **35**, 180–183.

Hacker B. R. and Christie J. M. (1991) Observational evidence for a possible new diffusion path. *Science* **251**, 67–70.

Hames W. E. and Hodges K. V. (1993) Laser 40Ar/39Ar argon evaluation of slow cooling and episodic loss of ^{40}Ar from a sample of polymetamorphic muscovite. *Science* **261**, 1721–1723.

Harrison L. G. (1961) Influence of dislocations on diffusion kinetics in solids with particular reference to the alkali halides. *Trans. Faraday Soc.* **57**, 1191–1199.

Harrison T. M. (1981) Diffusion of ^{40}Ar in hornblende. *Contrib. Mineral. Petrol.* **78**, 324–331.

Harrison T. M., Duncan I. and McDougall I. (1985) Diffusion of ^{40}Ar in biotite: temperature, pressure and compositional effects. *Geochim. Cosmochim. Acta* **49**, 2461–2468.

Hart E. W. (1957) On the role of dislocation in bulk diffusion. *Acta Metall.* **5**, 597.

Hodges K. V., Hames W. E. and Bowring S. A. (1994) ^{40}Ar–^{39}Ar age gradients in micas from a high-temperature low-pressure metamorphic terrain: evidence for very slow cooling and implications for the interpretation of age spectra. *Geology* **22**, 55–58.

Heber V. S., Brooker R. A., Kelley S. P. and Wood B. J. (2007) Crystal–melt partitioning of noble gases (helium, neon, argon, krypton, and xenon) for olivine and clinopyroxene. *Geochim. Cosmochim. Acta* **71**, 1041–1061.

Kelley S. P., Reddy S. M. and Maddock R. (1994) Laser-probe 40Ar–39Ar investigations of a pseudotachylyte and its host rock from the Outer Isles thrust, Scotland. *Geology* **22**, 443–446.

Kelley S. P. and Turner G. (1991) Laser probe ^{40}Ar/^{39}Ar measurements of loss profiles within individual hornblende grains from the Giants Range Granite, northern Minnesota, USA. *Earth Planet. Sci. Lett.* **107**, 634–648.

LeClaire A. D. (1963) The analysis of grain boundary diffusion measurements. *Br. J. Appl. Phys.* **14**, 351–356.

LeClaire A. D. and Rabinovitch A. (1981) A mathematical analysis of diffusion in dislocations I. Application to concentration 'tails'. *J. Phys. C: Solid State Phys.* **14**(27), 3863–3879.

LeClaire A. D. and Rabinovitch A. (1982) A mathematical analysis of diffusion in dislocations II. Influence at low densities on measured diffusion coefficients. *J. Phys. C: Solid State Phys.* **15**(16), 3455–3471.

LeClaire A. D. and Rabinovitch A. (1983) A mathematical analysis of diffusion in dislocations III. Diffusion in a dislocation array with diffusion zone overlap. *J. Phys. C: Solid State Phys.* **16**(11), 2087–2104.

LeClaire A. D. and Rabinovitch A. (1984) The mathematical analysis of diffusion in dislocations. In *Diffusion in Crystalline Solids* (eds. G. E. Murch and A. S. Nowick). Academic Press, Orlando, FL, pp. 257–318.

Lee J. K. W. (1995) Multipath diffusion in geochronology. *Contrib. Mineral. Petrol.* **120**, 60–82.

Onstott T. C., Phillips D. and Pringle-Goodell L. (1991) Laser microprobe measurement of chlorine and argon zonation in biotite. *Chem. Geol.* **90**(1–2), 25, 145–168.

Phillips D. and Onstott T. C. (1988) Argon isotopic zoning in mantle phlogopite. *GSA Bull.* **16**(6), 542–546.

Roselieb K., Blanc P., Buttner H., Jambon A., Rammensee W., Vielzeuf D. and Walter H. (1997) Experimental study of argon sorption in quartz: evidence for argon incompatibility. *Geochim. Cosmochim. Acta* **61**(3), 533–542.

Ruoff A. L. and Baluffi R. W. (1963) Strain enhanced diffusion in metals II: dislocation and grain-boundary short-circuiting models. *J. Appl. Phys.* **34**, 1848–1853.

Schärer U. and Allègre C. J. (1982) Uranium-lead system in fragments of a single zircon grain. *Nature* **295**, 585–587.

Schlegel M. L., Nagy K. L., Fenter P. L. and Sturchio N. C. (2002) Structures of quartz (1 0 1 0)– and (1 0 1 0)–water interfaces determined by X-ray reflectivity and atomic force microscopy of natural growth faces. *Geochim. Cosmochim. Acta* **66**, 3037–3054.

Scaillet S., Feraud G., Lagabrielle Y., Ballevre M. and Ruffet G. (1990) 40Ar/39Ar laser-probe dating by step-heating and spot fusion of phengites from the Dora Maira nappe of the Western Alps, Italy. *Geology* **18**, 741–744.

Scaillet S., Feraud G., Ballevre M. and Amouric M. (1992) Mg/Fe [(Mg, Fe)Si–Al_2]compositional control on argon behavior in high-pressure white micas: a 40Ar–-39Ar continuous laser-probe study from the Dora Maira nappe of the internal Western Alps, Italy. *Geochim. Cosmochim. Acta* **56**, 2851–2872.

Shiabata T., Takahashi E. and Ozima M. (1994) Noble gas partitioning between basaltic melt and olivine crystals at high pressures. In *Noble Gas Geochemistry and Cosmochemistry* (ed. J.-I. Matsuda). Terra Scientific, pp. 343–354.

Skrotzki W. (1990) Microstructures in hornblende of a mylonitic amphibolite. In *Deformation Mechanisms, Rheology, and Tectonics* (eds. R. J. Knipe and E. H. Rutter). Geol. Soc. London Spec. Pub 544.

Smoluchowski R. (1952) Movement and diffusion phenomena in grain boundaries. In *Imperfections in Nearly Perfect Crystals* (eds. W. Shockley, J. H. Holloman, R. Maurer and F. Seitz). Jon Wiley and Sons, New York, pp. 451–475.

Steurer W., Apfolter A., Koch M., Sarlat T., Søndergård E., Ernst W. E. and Holst B. (2007) The structure of the α-quartz (0 0 0 1) surface investigated using helium atom scattering and atomic force microscopy. *Surf. Sci.* **601**, 4407–4411.

Thomas J. B., Cherniak D. J. and Watson E. B. (2008) Lattice diffusion and solubility of argon in forsterite, enstatite, quartz and corundum. *Chem. Geol.* **253**, 1–22.

Turner G. (1968) The distribution of potassium and argon in chondrites. In *Origin and Distribution of Elements* (ed. L. H. Ahrens). Pergamon, New York, pp. 387–398.

Veblen D. R. and Buseck P. R. (1980) Microstructures and reaction mechanisms in biopyriboles. *Am. Mineral.* **65**, 599–623.

Wartho J.-A., Kelley S. P., Brooker R. A., Carroll M. R., Villa I. M. and Lee M. R. (1999) Direct measurement of Ar diffusion profiles in a gem-quality Madagascar K-feldspar using the ultra-violet laser ablation microprobe (UVLAMP). *Earth Planet. Sci. Lett.* **170**, 141–153.

Wartho J.-A., Kelley S. P. and Elphick S. C. (2005) Estimates of Ar diffusion and solubility in leucite and nepheline: electron microprobe imaging of Ar distribution in a mineral. *Am. Mineral.* **90**, 954–962.

Watson E. B. and Cherniak D. J. (2003) Lattice diffusion of Ar in quartz, with constraints on Ar solubility and evidence of nanopores. *Geochim. Cosmochim. Acta* **67**(11), 2043–2062.

Watson E. B., Thomas J. B. and Cherniak D. J. (2007) ^{40}Ar retention in the terrestrial planets. *Nature* **449**, 299–303.

Whipple R. T. P. (1954) Concentration contours in grain boundary diffusion. *Philos. Mag. 7th Ser.* **45**, 1225–1236.

Worden R. H., Walker F. D. L., Parrsons I. and Brown W. L. (1990) Development of microporosity, diffusion channels and deuritic coarsening in perthitic alkali feldspars. *Contrib. Mineral. Petrol.* **104**, 507–515.

Yund R. A., Smith B. M. and Tullis J. (1981) Dislocation-assisted diffusion of oxygen in albite. *Phys. Chem. Mineral.* **7**, 185–189.

Yund R. A., Quigley J. and Tullis J. (1989) The effect of dislocations on bulk diffusion in feldspars during metamorphism. *J. Met. Geol.* **7**, 337–341.

Yurimoto H. and Nagasawa H. (1989) The analysis of dislocation pipe radius for diffusion. *Mineral. J.* **14**, 171–178.

Yurimoto H., Morioka M. and Magasawa H. (1989) Diffusion in a single crystal of melilite: I. Oxygen. *Geochim. Cosmochim. Acta* **53**, 2387–2394.

Zhang X. Y., Cherniak D. J. and Watson E. B. (2006) Oxygen diffusion in titanite: lattice diffusion and fast-path diffusion in single crystals. *Chem. Geol.* **235**, 105–123.

Associate editor: Bjorn Mysen